Brief Communication: Mesoscale and submesoscale dynamics of marginal ice zone from sequential SAR observations

Igor E. Kozlov[1], Evgeny V. Plotnikov[1], Georgy E. Manucharyan[2]

[1]Remote Sensing department, Marine Hydrophysical Institute of RAS, Sevastopol, 299011, Russia

5   [2]School of Oceanography, University of Washington, Seattle, 98195-7940, United States of America

Correspondence to: Igor E. Kozlov (igor.eko@gmail.com)

Abstract. New possibility for horizontal current retrieval over marginal ice zone (MIZ) from sequential Sentinel-1 synthetic aperture radar (SAR) images is demonstrated. Daily overlapping SAR acquisitions made within 70-85° of latitude at time intervals <1 hour enable obtaining high-resolution velocity field and resolve MIZ dynamics down to submesoscales. An

10   example taken from the Fram Strait MIZ reveals energetic mesoscale and submesoscale eddies and filaments with horizontal velocities up to 0.75 m s^{-1}, strong sea ice convergence and high vorticity values. Such observations are critical to monitor the current and future state of marginal ice zones in the polar oceans.

1 Introduction

The width of the marginal ice zone (MIZ) in the polar oceans is rapidly growing over the past few decades (Strong and

15   Rigor, 2013). While being a region of strong lateral buoyancy gradients, energetic atmosphere-ice-ocean interactions and enhanced biological productivity, the MIZ is also a major source of errors in the long-term predictions of sea ice models (Tietsche et al., 2014).

MIZ dynamics and thermodynamics are critically affected by mesoscale and submesoscale eddies that exist in the MIZ interior and along the ice edge due to a multitude of possible mechanisms (e.g. Johannessen et al., 1987). Historical field

20   campaigns have documented the presence of mesoscale eddy-related motions down to several hundred meter depth with associated mean orbital speeds of about 0.5 m s^{-1} in the Fram Strait MIZ (Wadhams and Squire, 1983; Johannessen et al., 1987). These cyclonic ice-edge eddies not only swept ice away from the ice pack, but also entrained the warm Atlantic Water (AW) beneath the ice, causing an average ice edge melt at a rate of 1-2 km day^{-1} in summer (Johannessen et al., 1987). Eddies have also contributed to a nonuniform ice motion leading to significant ice deformation, thus, enhancing the melting

25   potential.

More recent model and field experiments also indicate very energetic motions associated with submesoscale eddies, fronts and filaments along the MIZ (Manucharyan and Thompson, 2017; von Appen et al., 2018; Swart et al., 2020) that importantly impact heat and carbon exchange between the ocean and atmosphere. In particular, submesoscale ocean flows induce large vertical velocities that can advect nutrients and relatively warm subsurface waters into the mixed layer with net

30   vertical heat fluxes toward the ice surface reaching 100 W m^{-2} (Manucharyan and Thompson, 2017). They also lead to enhanced mixing of water masses over short horizontal scales, importantly shaping the sea ice and biology structure within the MIZ (von Appen et al., 2018).

Surface signatures of MIZ eddies and filaments can be effectively traced in high-resolution synthetic aperture radar (SAR) images due to characteristic patterns formed by sea ice that mimics the ocean current structure beneath (Shuchman et al.,
35   1987; Kozlov et al., 2019). The manifestation of MIZ dynamics in SAR images is caused by the different level of radar backscatter from open water and low-concentration sea ice that tend to accumulate along the surface current convergence zones at eddy boundaries. Unlike the surfactant films marking eddy boundaries primarily under low winds (e.g. Karimova & Gade, 2016), SAR signatures of sea ice are well sustained even under high wind conditions (Johannessen et al., 1987) providing almost all-weather capability for monitoring MIZ dynamics. In regions with relatively low concentrations, sea ice
40   accumulates in predominantly cyclonic eddies and filaments, and the sea ice velocity becomes close to that of the surface ocean currents (Manucharyan & Thompson 2017), allowing one to make inferences about the upper ocean eddy dynamics from satellite sea ice observations.

Attempts to use spaceborne SAR data to retrieve sea ice motion in the polar oceans have been made since the launch of Seasat in 1978 (e.g. Hall and Rothrock, 1981), but relatively long sensing intervals (> 3 days) allowed to retrieve sea ice
45   motions at relatively large scales, O(50-100 km). Having optimum capabilities to observe polar regions independently on illumination and weather conditions, high-resolution SAR measurements are capable to resolve MIZ dynamics at significantly smaller scales, O(0.1-1 km), provided the time delay between sequential SAR images is sufficiently small, e.g. within 1-2 hours. However, until recently such a combination was not realized in practice for non-commercial SAR missions.

50   The aim of this letter is to demonstrate a new possibility for regular SAR observations over the large MIZ regions that has recently became available from sequential measurements of Sentinel-1 (hereinafter, S-1) A and B SAR missions launched in 2014 and 2016, respectively. As will be shown below, these data enable to retrieve high-resolution velocity field on a daily basis and observe MIZ dynamics down to submesoscales. We believe that this information is critical for better understanding of the key dynamical processes governing the submesoscale variability in MIZs, as well as for improving and validation of
55   sea ice and coupled ice-ocean models.

2 Data and methods

Since the launch of Sentinel-1B satellite in 2016, the SAR data from the two European polar-orbit S-1A and S-1B missions have become available for the public access. Each S-1 satellite carries C-band SAR instrument operating at multiple sensing modes each having a certain spatial resolution, range of incidence angles and set of polarization channels.

60   Due to their polar orbits, S-1 A and B have high measurement frequency over the high-latitude regions. Many of the S-1 images overlap within the latitude band 70-85° in the southern and northern hemispheres, forming a distinct set of sequential

SAR observations with a time lag of just around 50 minutes. As a result, from 2 to 4 overlapping scenes are available on a daily basis over the particular region of interest, for example over the Eurasian Arctic Ocean (Fig. 1, a). Fig. 1 (a) shows a map of the western Eurasian Arctic with locations of 43 S-1 A/B images available on 17 September 2017 at Copernicus

65   Open Access Hub (https://scihub.copernicus.eu). As is clearly seen, significant portions of the region, increasing northward, are covered by overlapping SAR data. Relatively short time lag between consecutive measurements, O(1 h), and high spatial resolution of SAR data, O(100 m), open up a unique opportunity to observe the MIZ dynamics on the daily basis.

To illustrate the potential of the data, here we analyze S-1 SAR images acquired in September 2017 over Fram Strait (FS) (green frame in Fig. 1, a), the region of quasi-permanent ice edge formed between the warm AW flowing northward into the

70   Arctic Ocean and cold ice-covered Polar Water (PW) flowing southward (von Appen et al., 2016). Copernicus Hub shows 120 SAR images available over FS in September 2017 with about half of them forming pairs of partly overlapping sequential images. In this work we focus on a pair of Sentinel-1 images acquired on September 17, 2017 at 07:12 UTC (S-1A) and at 8:00 UTC (S-1B) with a time lag of 48 minutes (Fig. 1, b). The data are gridded Level 1 Extra-Wide swath mode medium-resolution (~90 m) products covering an area of ~400×400 km at HH and HV polarisations. Dual-polarized HH-band is

75   further used for processing and analysis.

The procedure of velocity estimation from sequential SAR images has several main steps: i) image calibration for every image in the pair, ii) selection of overlapping image fragments, their normalization and filtering, iii) calculation of horizontal velocity field for image fragments using one of the methods for velocity estimation from image sequences (e.g. Emery et al., 1986; Chen, 2011; Marmorino and Chen, 2019). At first, S-1 images were calibrated to obtain normalized radar cross-section

80   units. Further, the overlapping fragments of both images in the pair were normalized to remove the signal trend in the range direction, and finally smoothed to reduce the speckle noise using the adaptive Wiener filter. For demonstration, here we use a maximum cross-correlation method (MCC) (Emery et al., 1986; Qazi et al., 2014) to retrieve surface velocity vectors over the MIZ. MCC was used with a moving window from 25×25 pixels for the initial large overlaps and down to 3×3 pixels for zooms over small-scale features with maximum allowed shifts up to 25 pixels in the zonal and meridional directions. For the

85   pixel size of 40 m, the resulting velocity fields were obtained at 1 km and ~100 m resolution, respectively. We also acknowledge that more elaborated alternative methods can be used for this purpose (see e.g. Chen, 2011; Marmorino and Chen, 2019). Given the spatial resolution of the SAR images of 88×87 m in range and azimuth directions, and the time lag between sequential images equal to 48 minutes, the velocity detection threshold in this case would be 0.03 m s^{-1}, similar to (Marmorino and Chen, 2019).

90   ## 3 Results

3.1 Structure of MIZ

The positions of two sequential S-1 SAR images acquired on September 17, 2017 over Fram Strait are shown in Fig. 1 (b). The area of the FS MIZ estimated directly from the SAR images is equal to ~115 km^2 with an average width of 60-70 km,

and possess a large number of small-to-mesoscale eddies, filaments and meanders. Figure 1 (c) shows an enlarged fragment
95 of the S-1A image which clearly shows the manifestation of an anomalously large anticyclonic vortex (marked as **A** in Fig.
1, c) with a diameter of about 80-90 km spreading southward out of the main MIZ over the depths of around 2000 m. One
can clearly see the formation of another smaller cyclonic vortex **C1** with a diameter of about 15 km on the western periphery
of **A**. Many other small-scale eddies and meanders O(1 km) are seen along its periphery (Fig. 1, c). Notably, the periphery of
the anticyclone **A** is bounded by several curved ice-filled narrow filaments, while a lot of open water with dispersed low-
100 concentration ice fields is found in the center. This is opposite for the cyclonic eddies **C1** and **C2** with more ice accumulated
in their centers, in agreement with model results of Manucharyan and Thompson (2017).

3.2 Velocity retrieval over MIZ

A fragment of the SAR image presented in Fig. 1 (c) was further used for surface current retrieval using MCC method.
According to WindSat and ASCAT scatterometers' data for 17 September 2017 (not shown), the near-surface wind field was
105 characterized by south-easterly winds of 3-5 m s^{-1}, meaning that the ice drift near the ice edge should reflect the underlying
ocean circulation (Shuchman et al., 1987; Manucharyan and Thompson, 2017).

Fig. 2 (a) shows the resulting velocity field obtained for the initial image fragment with the large anticyclonic vortex **A**. The
overall geometry of the obtained current field is in a good agreement with the ice structures seen in the SAR image, and
shows a pronounced anticyclonic rotation associated with the large vortex **A**. The modulus of horizontal current velocity $|\boldsymbol{u}|$,
110 comprised of the eastward u and the northward v velocity components, is shown in Figure 2 (b). As seen, a general
southeastward drift of the MIZ with an average velocity of 0.2-0.3 m s^{-1} is seen in the upper part of the image. It increases in
the middle of the scene and forms a strong southward jet with current velocities reaching 0.75 m s^{-1}. This jet-like structure
then evolves into large anticyclone **A** downstream. The mean orbital velocity of vortex **A** is about 0.4-0.5 m s^{-1}. However,
the maximum values attain 0.65-0.75 m s^{-1} along its north-western periphery and 0.5 m s^{-1} along its southern boundary,
115 gradually decreasing toward the center (Fig. 2, b). Such high velocity values are confirmed by the manual analysis of
horizontal shifts of individual ice floes in sequential images (not shown).

Fig. 3 (a) shows the velocity field for the enlarged SAR fragment over the western part of the anticyclone **A**. A number of
distinct dynamic features is seen along its periphery including cyclonic vortex **C1** and narrow elongated filaments **F1** and
F2. As seen from Fig. 3 (a), all these features are well manifested in the SAR image due to enhanced radar backscatter from
120 sea ice. The latter is accumulated within narrow surface current convergence zones associated with ageostrophic secondary
circulation near submesoscale fronts and filaments (McWilliams, 2016). The field of horizontal divergence, $\nabla \cdot \boldsymbol{u} = \partial u / \partial x + \partial v / \partial y$, confirms the formation of strong convergence zones up to -5×10^{-4} s^{-1} (blue color in Fig. 3, b) that
correspond to bright sea ice patterns seen in the SAR image (Fig. 3, a).

As noted above, the periphery of the anticyclone **A** is bounded by several narrow filaments (Fig. 3, a). Filament **F1** is 0.5-1.5
125 km wide and ~60 km long, very similar to the submesoscale cyclonic filament sampled in detail in the Fram Strait MIZ by
von Appen et al. (2018). However, as both the interpretation of the SAR image and the retrieved current velocity suggest,

this filament is not a stand-alone feature, but is a part of the larger eddy-induced frontogenesis pattern and, hence, cannot be interpreted out of the context. The important consequence is that its movement direction and, hence, the sign of relative vorticity, $\zeta = \partial v/\partial x - \partial u/\partial y$, is different depending on its part to be considered (Fig. 3, c).

130   The data show that **F1** is stretching along-front into the opposite directions and moves northward with a mean (maximum) speed of 0.4-0.5 (0.75) m s⁻¹ in its upper half, while drifting southward at an average (maximum) velocity of 0.3-0.4 (0.55) m s⁻¹ in the lower part, as shown by arrows in Fig. 3 (a). The cross-front velocity is almost negligible in its southern and northern parts, while it attains ~0.05-0.1 m/s near the divergence point (found next to **F1** notion in Fig. 3, a). The relative vorticity ζ values estimated for the mean current velocity $\Delta v = 0.4$ m s⁻¹ and characteristic filament cross-front width $\Delta x =$

135   1 km are $\zeta = \Delta v/\Delta x = {\sim}3f$, where f is the Coriolis parameter equal $f = 1.433 \cdot 10^{-4} s^{-1}$ for latitude $\theta = 80.2°$ N. This gives the Rossby number $Ro = \zeta/f \sim O(1)$, clearly indicating a submesoscale nature of this filament. Similar stretching and movement into the opposite directions are also observed for the filament **F2**, which also splits into cyclonic and anticyclonic counterparts (Fig. 3, c). Its cyclonic part starts to meander and then rotates anticlockwise to shape the boundary of the cyclone **C1**.

140   The shape of the cyclone **C1**, defined from the orientation of the bounding ice streaks, is highly elliptical with minor axis being about 10 km and major – about 25 km (Fig. 3, a). The associated orbital velocities are 0.2-0.65 m s⁻¹ (mean value 0.5 m s⁻¹), being largest along its major axis on the western and eastern sides, and smallest near the eddy center. The horizontal divergence field shows high negative values (convergence) where sea ice accumulates along the eddy boundaries (compare Figs. 3a and 3b). As noted above, the ice concentration at the boundaries and in the center of **C1** is higher than for eddy **A**.

145   This is confirmed by the more intense surface convergence over **C1** (Fig. 3, b) that is presumably linked to stronger ageostrophic motions. Indeed, the comparison of vorticity values for eddies **A** ($\zeta \approx 0.07f$) and **C1** ($\zeta \approx 0.3f$) shows a higher Rossby number for the cyclone **C1** with ageostrophic effects playing a higher role in this case.

Fig. 3 (d) shows the field of instantaneous kinetic energy (KE), $KE = \frac{1}{2}(u^2 + v^2)$. In general, one may see a very energetic patterns associated with eddy dynamics in the MIZ. As seen, the maximum of the KE reaches 0.23 m² s⁻² over the northern

150   periphery of **A** with the mean value of about 0.1 m² s⁻². For the cyclone **C1**, it is slightly less, but still high. The maximum value of 0.2 m² s⁻² is found over the western periphery of **C1**, while over the eastern part it is about 0.1-0.15 m² s⁻².

4 Discussion and conclusions

In this letter we demonstrate a new possibility to retrieve horizontal velocity field from sequential Sentinel-1 SAR images taken over low-concentration ice regions of polar oceans where sea ice motion is indicative of mesoscale and submesoscale

155   eddies and filaments. The pair of S-1 SAR images acquired over the Fram Strait MIZ reveals a large anticyclonic ice-edge eddy of 80-90 km in diameter and numerous cyclonic eddies of smaller size at its periphery, bounded by several elongated ice-filled filaments. The reconstructed currents show that maximum orbital velocities of the large anticyclone exceed 0.7 m s⁻¹. While historic field campaigns have documented the generation of ice-edge eddies in central Fram Strait (e.g. Wadhams

The Cryosphere
Discussions

Open Access

EGU

and Squire, 1983; Johannessen et al., 1987; Shuchman et al., 1987), the observations of such an anomalously large and
160   energetic MIZ eddy in the Arctic Ocean have never been reported before.

Notably, the location of MIZ eddies reported here coincides with the ice edge region in central FS characterized by high
summer-time eddy kinetic energy (EKE) values (exceeding 200 cm^{-2} s^{-2}) reported by Bulczak et al. (2014) based on satellite
altimetry data, and later confirmed by long-term mooring observations (von Appen et al., 2016). Such anomalously high
EKE values relative to adjacent regions were attributed to the complex atmosphere-ice-ocean interplay, including the
165   formation of eddies due to barotropic and baroclinic instability of an ice edge jet along the MIZ, topographic generation and
trapping, interaction of AW eddies advected to the ice edge with meltwater fronts, wind-induced differential Ekman
pumping along a meandering ice edge, or their combinations (Johannessen et al., 1987). The lifetime of such eddies was
reported to be at least 20-30 days with diameters ranging within 20-40 km, rarely reaching 60 km (Wadhams and Squire,
1983). In our case, surface signatures of the large anticyclone were clearly seen only for about 10 days from 14 September
170   until 24 September 2017, when it became fully ice-filled and indiscernible from the main MIZ region.

The SAR data also reveals the development of several elongated filaments and smaller-scale cyclones on the periphery of the
large anticyclone. The latter is frequently reported in literature (e.g. Zatsepin et al., 2019) and is attributed to horizontal shear
instability of anticyclonic flows very effective to produce submesoscale cyclones (McWilliams, 2016). Analysis of the
reconstructed current velocity and the filament length scale clearly shows submesoscale nature of these features with vertical
175   vorticity being about three times the Coriolis frequency. Similarly, strong filaments were recently reported by von Appen et
al. (2018) based on detailed field observations in central FS, showing that in regions where AW and PW meet such filaments
could be deep reaching with density anomaly extending down to 400 m depth, potentially influencing biomass and nutrient
distributions in the water column.

As revealed from SAR data, these elongated filaments move at the maximum speed of 0.75 m s^{-1}, being a part of the larger
180   eddy-induced frontogenesis pattern. They are stretching and moving into the opposite directions, delineating a dipole eddy
structure with opposite vorticity sign. Due to their large spatial extent in the along-front direction, such peculiarities of the
submesoscale flow could be hardly resolved even in specialized high-resolution field observations, when a different velocity
structure would be inferred *in situ* depending on the measurement location relative to the filament part. The latter clearly
emphasizes the capability of high-resolution sequential SAR data to resolve small-scale peculiarities of the complex MIZ
185   dynamics. Given the abundance of MIZ eddies and fronts in the Arctic and Southern Oceans (Kozlov et al., 2019; Swart et
al., 2020; von Appen et al., 2018), these energetic features may importantly influence vertical heat transport toward the sea
ice and ice melt, upper ocean stratification and distribution of nutrients and buoyant materials in the water column.

Apart from its potential use in validation and improvement of sea ice forecasting models, the availability of daily regular
high-resolution sequential Sentinel-1 SAR observations could contribute to advancing our understanding of multi-scale
190   atmosphere-ice-ocean interactions in the marginal ice zones, identifying hot-spots of high kinetic energy, and quantifying
lateral and vertical dispersion of various buoyant materials, including microplastics and oil pollution in the polar oceans.

Acknowledgments

References

Bulczak, A. I., Bacon, S., Naveira Garabato, A. C., Ridout, A., Sonnewald, M. J., and Laxon, S. W.: Seasonal variability of sea surface height in the coastal waters and deep basins of the Nordic Seas, Geophys. Res. Lett., 42, 113–120,

200   https://doi.org/10.1002/2014GL061796, 2015.

Chen, W.: Nonlinear inverse model for velocity estimation from an image sequence, J. Geophys. Res., 116 (06015), https://doi.org/10.1029/2010JC006924, 2011.

Emery, W. J., Thomas, A. C., Collins, M. J., Crawford, W. R., and Mackas, D. L.: An objective method for computing advective surface velocities from sequential infrared satellite images, J. Geophys. Res., 91(C11), 12865–12878,

205   https://doi.org/10.1029/JC091iC11p12865, 1986.

Hall, R. T., and Rothrock, D. A.: Sea ice displacement from Seasat synthetic aperture radar, J. Geophys. Res., 86(C11), 11078–11082, https://doi.org/10.1029/JC086iC11p11078, 1981.

Johannessen, J. A., Johannessen, O. M., Svendsen, E., Shuchman, R., Manley, T., Campbell, W. J., Josberger, E. G., Sandven, S., Gascard, J. C., Olaussen, T., Davidson, K., and Van Leer, J.: Mesoscale eddies in the Fram Strait marginal ice

210   zone during the 1983 and 1984 Marginal Ice Zone Experiments, J. Geophys. Res.: Oceans, 92(C7), 6754-6772, https://doi.org/10.1029/JC092iC07p06754, 1987.

Karimova, S. and Gade, M.: Improved statistics of sub-mesoscale eddies in the Baltic Sea retrieved from SAR imagery, Int. J. Remote Sens, 37, 2394–2414, https://doi.org/10.1080/01431161.2016.1145367, 2016.

Kozlov, I. E., Artamonova, A. V., Manucharyan, G. E., and Kubryakov, A. A.: Eddies in the Western Arctic Ocean from

215   spaceborne SAR observations over open ocean and marginal ice zones, J. Geophys. Res.: Oceans, 124(9), 6601-6616, https://doi.org/10.1029/2019JC015113, 2019.

Manucharyan, G. E. and Thompson, A. F.: Submesoscale sea ice–ocean interactions in marginal ice zones, J. Geophys. Res.: Oceans, 122(12), 9455-9475, https://doi.org/10.1002/2017JC012895, 2017.

Marmorino, G., and Chen, W.: Use of WorldView-2 Along-Track Stereo Imagery to Probe a Baltic Sea Algal Spiral, Remote

220   Sens., 11(7), 865, https://doi.org/10.3390/rs11070865, 2019.

McWilliams, J. C.: Submesoscale currents in the ocean, Proc. Royal Soc. A. 472 (2189). https://doi.org/10.1098/rspa.2016.0117, 2016.

Mensa, J. A., Timmermans, M.-L., Kozlov, I. E., Williams, W. J., and Özgökmen, T.: Surface drifter observations from the Arctic Ocean's Beaufort Sea: Evidence for submesoscale dynamics. J. Geophys. Res.: Oceans, 122(12), 9455–9475,

225 https://doi.org/10.1002/2017JC013728, 2018.

Qazi, W. A., Emery, W. J., and Fox-Kemper, B.: Computing ocean surface currents over the coastal California current system using 30-min-lag sequential SAR images, IEEE Trans. Geosci. Rem. Sens., 52, 7559–7580, doi:10.1109/TGRS.2014.2314117, 2014.

Shuchman, R. A., Johannessen, O. M., Campbell, W. J., Lannelongue, N., Burns, B. A, Josberger, E. G., and Manley, T.:

230 Remote sensing of the Fram Strait marginal ice zone. Science, 236, 427–439. https://doi.org/10.1126/science.236.4800.429, 1987.

Strong, C., and Rigor, I. G., Arctic marginal ice zone trending wider in summer and narrower in winter, Geophys. Res. Lett., 40, 4864– 4868, https://doi.org/10.1002/grl.50928, 2013.

Swart, S., du Plessis, M. D., Thompson, A. F., Biddle, L. C., Giddy, I., Linders, T., Mohrmann, M. and Nicholson, S. A.:

235 Submesoscale fronts in the Antarctic marginal ice zone and their response to wind forcing, Geophys. Res. Lett., 47, e2019GL086649, https://doi.org/10.1029/2019GL086649, 2020.

Tietsche, S., Day, J. J., Guemas, V., Hurlin, W. J., Keeley, S. P. E., Matei, D., Msadek, R., Collins, M. and Hawkins, E.: Seasonal to interannual Arctic sea ice predictability in current global climate models. Geophys. Res. Lett., 41, 1035–1043. https://doi.org/10.1002/2013GL058755, 2014.

240 von Appen, W. J. V., Schauer, U., Hattermann, T., and Beszczynska-Möller, A.: Seasonal cycle of mesoscale instability of the West Spitsbergen Current, J. Phys. Oceanogr., 46(4), 1231-1254, https://doi.org/10.1175/JPO-D-15-0184.1, 2016.

von Appen, W. J., Wekerle, C., Hehemann, L., Schourup-Kristensen, V., Konrad, C., and Iversen, M. H.: Observations of a submesoscale cyclonic filament in the marginal ice zone. Geophys. Res. Lett., 45(12), 6141-6149, https://doi.org/10.1029/2018GL077897, 2018.

245 Wadhams P., Squire V. A., An ice-water vortex at the edge of the East Greenland Current, J. Geophys. Res., 88(C5), 2770– 2780, https://doi.org/10.1029/JC088iC05p02770, 1983.

Zatsepin, A., Kubryakov, A., Aleskerova, A., Elkin, D. and Kukleva, O.: Physical mechanisms of submesoscale eddies generation: evidences from laboratory modeling and satellite data in the Black Sea. Ocean Dyn. 69, 253–266, https://doi.org/10.1007/s10236-018-1239-4, 2019.

250
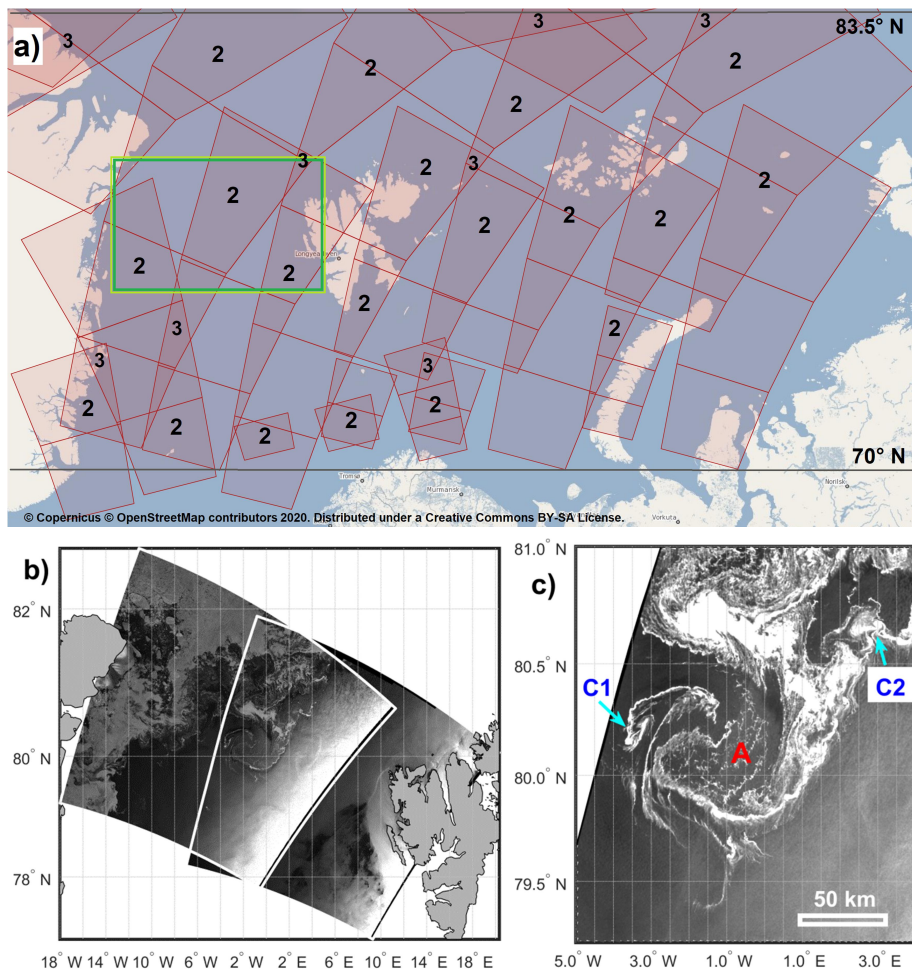
Figure 1: a) Map of the western Eurasian Arctic showing the acquisition tracks of Sentinel-1 A/B SAR images available on 17 September 2017. Pink frames mark the borders of individual SAR images, while digits show the number of overlapping SAR frames. Grey lines mark latitude boundaries of 70° N and 83.5° N. Green box shows the area of Fram Strait. The map is taken from Copernicus Open Access Hub © Copernicus © OpenStreetMap 2020. Distributed under a Creative Commons BY-SA License. **b)** Position of two sequential Sentinel-1 A/B images acquired on September 17, 2017 over Fram Strait. **c)** Enlarged fragment of Sentinel-1A image for the same date (07:12 UTC) with distinct signatures of a large anticyclone and several cyclones in the marginal ice zone. Letters A, C1, C2 mark eddies described in the text.
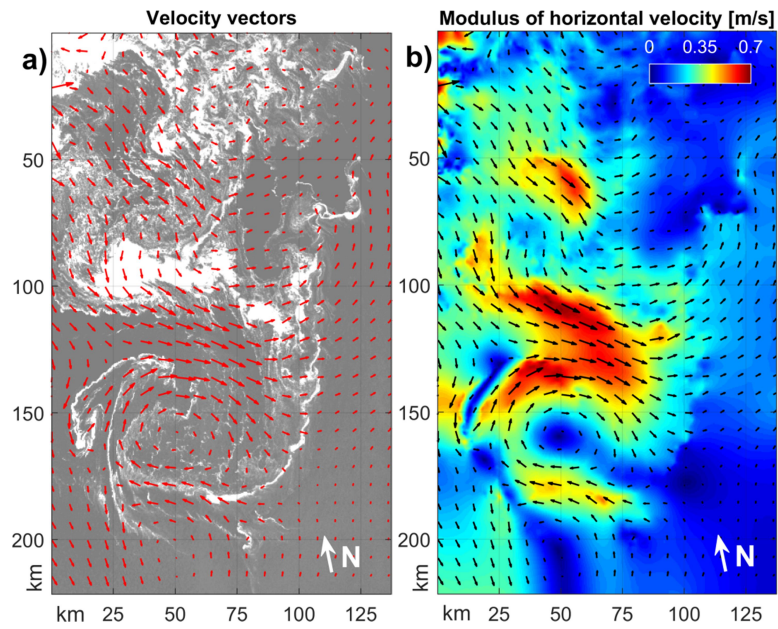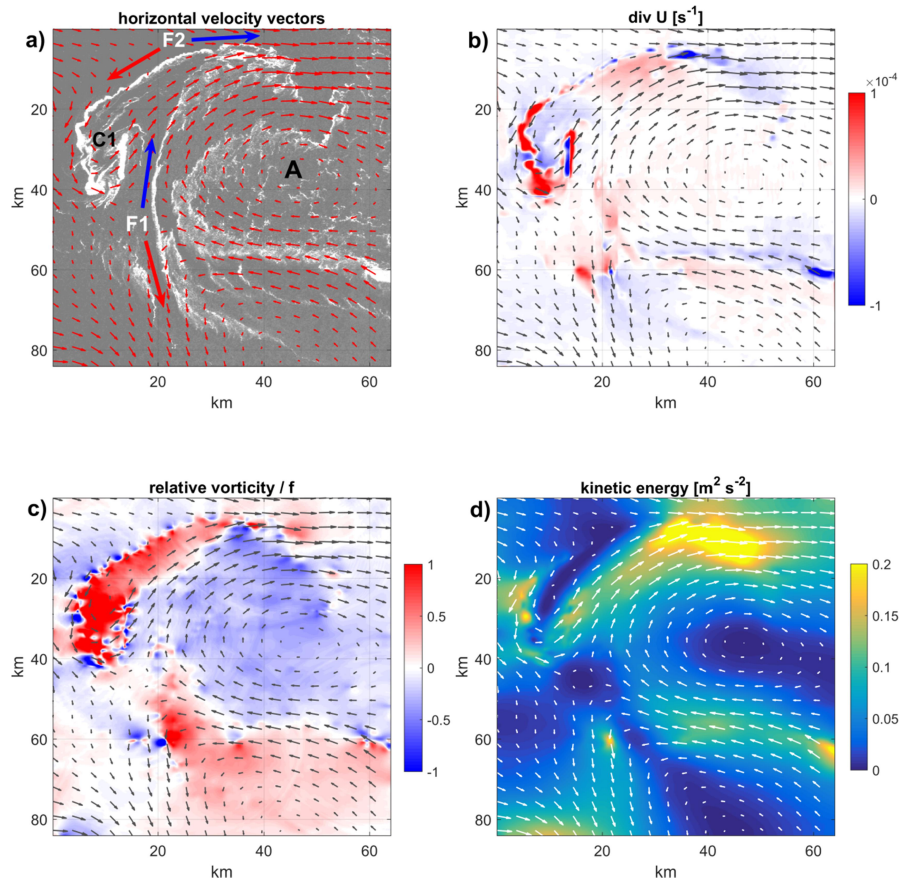
Figure 2: The horizontal velocity vectors calculated from two sequential Sentinel-1 A/B images taken on September 17, 2017 over Fram Strait using MCC method superimposed on a) the SAR image and b) modulus of the horizontal velocity.

Figure 3: Results for zoomed area over anticyclone A and cyclone C1: (a) horizontal velocity vectors; (b) horizontal divergence, (c) relative vorticity divided by the Coriolis parameter; (d) kinetic energy. The largest vector in (a) has a magnitude of 0.75 m s⁻¹. Letters A, C1, F1 and F2 in c) mark the locations of the eddies and filaments described in the text, while blue and red arrows show the movement direction of the filaments F1 and F2.